

## Revitalizing E-waste: Eco-friendly electrochemical sensor for Hg(II) detection enhanced by oxygen vacancy in metal oxide nanostructures based on recycled LCD

Maroua Saadaoui, Assem T. Mohamed, Abdul Hakeem Anwer, Siham Y. Al-Qaradawi, Mazen Khaled, Abdelbaki Benamor

### Item type

Journal Contribution

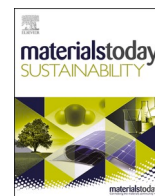
### Terms of use

This work is licensed under a [CC BY 4.0](https://creativecommons.org/licenses/by/4.0/) license

### This version is available at

[https://manara.qnl.qa/articles/journal\\_contribution/Revitalizing\\_E-waste\\_Eco-friendly\\_electrochemical\\_sensor\\_for\\_Hg\\_II\\_detection\\_enhanced\\_by\\_oxygen\\_vacancy\\_in\\_metal\\_oxide\\_nanostructures\\_based\\_or](https://manara.qnl.qa/articles/journal_contribution/Revitalizing_E-waste_Eco-friendly_electrochemical_sensor_for_Hg_II_detection_enhanced_by_oxygen_vacancy_in_metal_oxide_nanostructures_based_or)  
Access the item on Manara for more information about usage details and recommended citation.

Posted on Manara – Qatar Research Repository on  
2025-03-01



# Revitalizing E-waste: Eco-friendly electrochemical sensor for Hg(II) detection enhanced by oxygen vacancy in metal oxide nanostructures based on recycled LCD

Maroua Saadaoui<sup>a</sup>, Assem T. Mohamed<sup>a</sup>, Abdul Hakeem Anwer<sup>a</sup>, Siham Y. Al-Qaradawi<sup>c</sup>, Mazen Khaled<sup>c</sup>, Abdelbaki Benamor<sup>a,b,\*</sup>

<sup>a</sup> Gas Processing Center, College of Engineering, Qatar University, P. O. Box 2713, Doha, Qatar

<sup>b</sup> Department of Chemical Engineering, College of Engineering, Qatar University, P.O.Box 2713, Doha, Qatar

<sup>c</sup> Department of Chemistry & Earth Sciences, College of Arts and Sciences, Qatar University, P.O.Box 2713, Doha, Qatar

## ARTICLE INFO

### Keywords:

Electrochemical sensor  
Recycled LCD  
CeO<sub>2</sub>-Co<sub>3</sub>O<sub>4</sub>  
Mercury detection  
Sea water

## ABSTRACT

In the current work, an innovative eco-friendly sensor using ceria integrated cobalt oxide nanosheets immobilized on LCD monitor (Ce@Co-EcoR) recycled from E-waste is presented. The Ce@Co-EcoR nanocomposite was thoroughly investigated using appropriate characterization techniques. This nanostructured electrode was employed to construct an electrochemical sensor to detect mercury. It showed a very low detection limit of 2.8 ppb, a wide detection ranges from 16 to 620 ppb, and a good sensitivity of 158.28  $\mu\text{A cm}^{-2}\text{ppm}^{-1}$ . The sensor applicability was verified by performing interference, repeatability, stability studies. It was also applied to control the purity of sea water. This work underscores the potential of incorporating recycled materials onto sensor technology, not only to control environmental pollution, but also to promote sustainable practices in scientific innovation.

## 1. Introduction

In recent years, the extensive discharge of pollutants into ecosystems has become a significant global concern, especially impacting water, a crucial natural resource. The release of toxic heavy metals through wastewater further exacerbates environmental degradation, threatening the integrity of ecosystems worldwide [1]. These metals are assimilated by aquatic flora and fauna, leading to bioaccumulation and posing indirect risks to human health through trophic transfer [2]. Notably, mercury detection is paramount for monitoring environmental quality, especially in light of escalating pollution levels driven by rapid urbanization and industrialization. In coastlines, mercury compounds continuously enter marine ecosystems [3], with levels reaching as high as 15 million tons [4]. Mercury, recognized as the most pernicious heavy metal even at trace levels [5], can severely impact human health, affecting the central nervous, immunological systems, respiratory, and gastrointestinal, and causing conditions such as memory impairment and sensory deficits [6]. To address these detrimental effects, governing bodies such as the Environmental Protection Agency (EPA) and the World Health Organization (WHO) have defined thresholds for Hg<sup>2+</sup>

ions in freshwater, typically falling between 10.0 and 30.0 nM [7]. Consequently, the development of highly sensitive methodologies for detecting trace concentrations of mercury is of paramount importance. Among the diverse methodologies for detecting trace heavy metal ions, electrochemical detection is broadly known for its exceptional sensitivity, low detection limits, and rapid response times [2]. This technique involves the measurement of electrical signals generated by the interaction of heavy metal ions with an electrode surface. Despite its extensive application, a significant portion of current research is predominantly empirical, lacking a systematic approach to electrode design.

Utilizing electrodes manufactured from E-waste recycled materials ("EcoR" electrode) offers a sustainable and cost-effective solution for advancing green technologies. This approach not only limits the dissemination of e-waste—projected to reach approximately 74 million metric tons globally by 2030—but also promotes sustainability by repurposing materials that would otherwise contribute to environmental pollution [8]. LCDs are hazardous due to their content of toxic substances like PBDEs (flame retardants in consumer products), PBBs (toxic brominated flame retardants), and various heavy metals such as

\* Corresponding author. Gas Processing Center, College of Engineering, Qatar University, P. O. Box 2713, Doha, Qatar.

E-mail address: [benamor.abdelbaki@qu.edu.qa](mailto:benamor.abdelbaki@qu.edu.qa) (A. Benamor).

<https://doi.org/10.1016/j.mtsust.2024.101015>

Received 10 September 2024; Received in revised form 3 October 2024; Accepted 21 October 2024

Available online 22 October 2024

2589-2347/© 2024 The Authors. Published by Elsevier Ltd. This is an open access article under the CC BY license (<http://creativecommons.org/licenses/by/4.0/>).

mercury arsenic, lead, chromium, and cadmium [9]. E-waste, particularly from liquid crystal displays (LCDs), offers a valuable platform for reuse as direct electrodes. Recycling LCD screens poses an environmental challenge; however, their potential use as electrodes for constructing electrochemical sensors offers a promising solution [10]. Nevertheless, bare LCDs are not particularly effective in detecting a range of heavy metal ions. To address this, modifying LCD electrodes with nanomaterials, which provide highly active sites, can significantly enhance their performance.

Metal oxide-based electrochemical sensors stand out among various nanomaterials due to their exceptional performance, simplicity in preparation, and cost-effectiveness [11]. Despite these advantages, pure metal oxides often lack the necessary electrical conductivity to achieve the high sensitivity required for effective electrochemical detection. Therefore, enhancing the surface of metal oxides with additional active sites is essential to improve the detection capabilities of these sensors. Cobalt oxide ( $\text{Co}_3\text{O}_4$ ) is well-known as an ideal electrode material for sensors due to its unique features, such as its intercalation morphologies, reversible redox properties ( $\text{Co}^{2+} \leftrightarrow \text{Co}^{3+}$ ), and a large theoretically specific capacity around  $3560 \text{ F g}^{-1}$  [12]. These properties enhance charge transfer at the electrode-electrolyte interface, facilitating greater signal amplification and detection sensitivity. Therefore,  $\text{Co}_3\text{O}_4$  significantly improves the performance of electrochemical sensors [13]. Scientists have extensively explored binary and ternary combinations of  $\text{Co}_3\text{O}_4$  with various heterogeneous materials, particularly focusing on the synergistic effects of introducing oxygen vacancies [14].

The development of oxygen vacancies on nanometal oxide surfaces is critical because it generates new active sites that enhance electrical conductivity. These vacancies accelerate electron conduction rates, facilitate redox reactions, and improve the ability of nanometal oxides to adsorb mercury ions. For example, Parwaiz et al. developed cobalt-doped ceria on reduced graphene, showcasing its efficiency as an electrocatalyst in oxygen reduction reactions [15]. This research underscores the favorable characteristics of  $\text{CeO}_2$ , such as its unique cubic configuration, ability to transition between different “oxidation states” and its narrow “band gap” [16]. Additionally, the incorporation of graphene quantum dots into the Ce–ZnO nanofibers increases the oxygen vacancy sites, allowing the selective detection of  $\text{Hg}^{2+}$  ions via the differential pulse voltammetry technique. The electrode achieved a limit of detection (LOD) value of 267 nM within a current range of 0.1 and 100  $\mu\text{M}$  [17]. Furthermore, iron-doped  $\text{TiO}_2$  nanoparticles, which creates numerous oxygen vacancies, generally promotes the formation of abundant hydroxyl groups ( $\text{OH}^-$ ) in water, thereby efficiently capturing  $\text{Hg}(\text{II})$  ions. This emphasizes the significant role of doping transition metals with variable valence states to regulate oxygen vacancy concentrations and effectively activate inert metal oxides [18].

In this study, we design an innovative electrochemical sensor employing cobalt and ceria oxides in the form of nanoparticles and thin films. These materials serve as effective modifiers of “EcoR” electrodes, providing easy platforms for detecting mercury using square wave stripping voltammetry (SWSV). The optimized sensor design was successfully validated by monitoring mercury levels in seawater. This approach not only addresses the recycling issue but also promotes sustainability and cost-efficiency in environmental monitoring technologies.

## 2. Experimental methodology

### 2.1. Chemical reagents

All reagents: mercury (II)nitrate-1-hydrate ( $\text{Hg}(\text{NO}_3)_2$ , 99%), Ce (III)-nitrate hexahydrate ( $\text{Ce}(\text{NO}_3)_3 \cdot 6\text{H}_2\text{O}$ , 99%), cobalt(II)-nitrate hexahydrate ( $\text{Co}(\text{NO}_3)_2 \cdot 6\text{H}_2\text{O}$ ,  $\geq 98\%$ ), Potassium phosphate monobasic ( $\text{KH}_2\text{PO}_4$ ,  $\geq 98\%$ ), Potassium chloride ( $\text{KCl}$ ,  $\geq 98\%$ ) and sodium chloride ( $\text{NaCl}$ ,  $\geq 98\%$ ) were purchased from GPR. Hydrochloric acid ( $\text{HCl}$ , 35–38%) was obtained from qualikems. Sodium phosphate dibasic

( $\text{Na}_2\text{HPO}_4$ ,  $\geq 98\%$ ), Potassium ferricyanide ( $\text{K}_3[\text{Fe}(\text{CN})_6]$ ,  $\geq 99.0\%$ ) and Potassium hexacyanoferrate(II) trihydrate ( $\text{K}_3[\text{Fe}(\text{CN})_6]$ ,  $\geq 99.0\%$ ) were acquired from Sigma Aldrich. The production of all solutions included the use of ultrapure water with a resistivity less than 18.18  $\text{M}\Omega \text{ cm}$ , which was obtained by a Milli-Q system. The solvents were obtained from VWR chemicals.

### 2.2. Preparation of the nanostructured electrodes

#### 2.2.1. Extraction of LCD and prepare an electrode

The LCD monitor was extracted from the TV screen produced by TCL. Its outer screen remained intact and devoid of any scratches. Using a cutter pen, the black-colored section was sliced into pieces roughly 1 cm wide and 1.5 cm long. To ascertain its conductivity, a digital multimeter was employed, utilizing the conducting side for electrode preparation. Subsequently, EcoR (the extracted part of LCD) was subjected to the nanostructuration.

#### 2.2.2. High-precision electrodeposition: crafting cobalt oxide on LCD

The  $\text{Co}_3\text{O}_4$ -EcoR was prepared applying a simple electrodeposition process represented in Fig. 1 (A). Before the deposition of cobalt oxide, the -EcoR underwent sequential cleaning in ethanol, acetone and distilled water. Afterwards,  $\text{Co}(\text{OH})_2$  nanosheets were electrochemically deposited onto the surface of the LCD. This coating occurred at a potential of  $-1.25\text{V}$  (vs  $\text{AgCl}/\text{Ag}$ ) in 0.1 M aqueous solution of  $\text{Co}(\text{NO}_3)_2$ . Then, the cobalt film was cleaned with ethanol and dried at room temperature.

#### 2.2.3. Integration of $\text{CeO}_2$ on Co-EcoR electrode

$\text{CeO}_2$  was progressively coated onto the cobalt film, utilizing the sonication method [19]. Under ambient conditions, the sonicator probe was immersed into solution consisting of 0.75 mM of  $\text{Ce}(\text{NO}_3)_3$ , along with the LCD slides previously modified by the cobalt film, during 20 min. The modified electrodes were then subjected to an annealing process, that included raising the temperature from the surroundings to 300 °C. To ensure that oxides would develop within the nanomaterials, this temperature was maintained for 2 h.

### 2.3. Characterization

Scanning electron microscopy (SEM) using a JEOL JSM-67001 instrument was used to examine the surface morphology of the nanostructured electrodes at different stages of their development. Transmission Electron Microscopy (TEM): TECNAI G2 TEM and TF20 was employed to analyze the particle size and morphology of the samples. In order to make the samples, a minute quantity of catalyst powder, weighing a few milligrams, was subjected to sonication in n-propane. Subsequently, a small droplet of the resulting suspension was carefully deposited onto a copper grid with a 200-mesh size. Surface chemical analysis of the LCD was achieved using X-ray photoelectron spectroscopy (XPS) with a Kratos AXIS Ultra DLD spectrometer, both before and after modification. Preceding to the XPS study, the sample upper layer was cleaned with an Ar ion-gun operating at 4 kV. X-ray diffraction (XRD) profiles were gathered utilizing a “Rigaku-MiniFlex-600” benchtop diffractometer to assess the overall crystalline phase composition of the nanomaterials. This instrument, equipped with a Cu K $\alpha$  radiation source functioning at 15 mA and 30 kV, collected data over a 2 $\theta$  range of approximately 5–80° at a scanning speed of 4° per minute.

### 2.4. Electrochemical analysis techniques

The electrochemical performance of the fabricated electrodes was assessed using a Gamry Reference 600 electrochemical workstation. All experiments utilized a three-electrode cell setup, consisting of the developed LCD-based (EcoR) working electrode, an  $\text{Ag}/\text{AgCl}/\text{KCl}$  (3 M) reference electrode, and a platinum wire as the counter electrode.

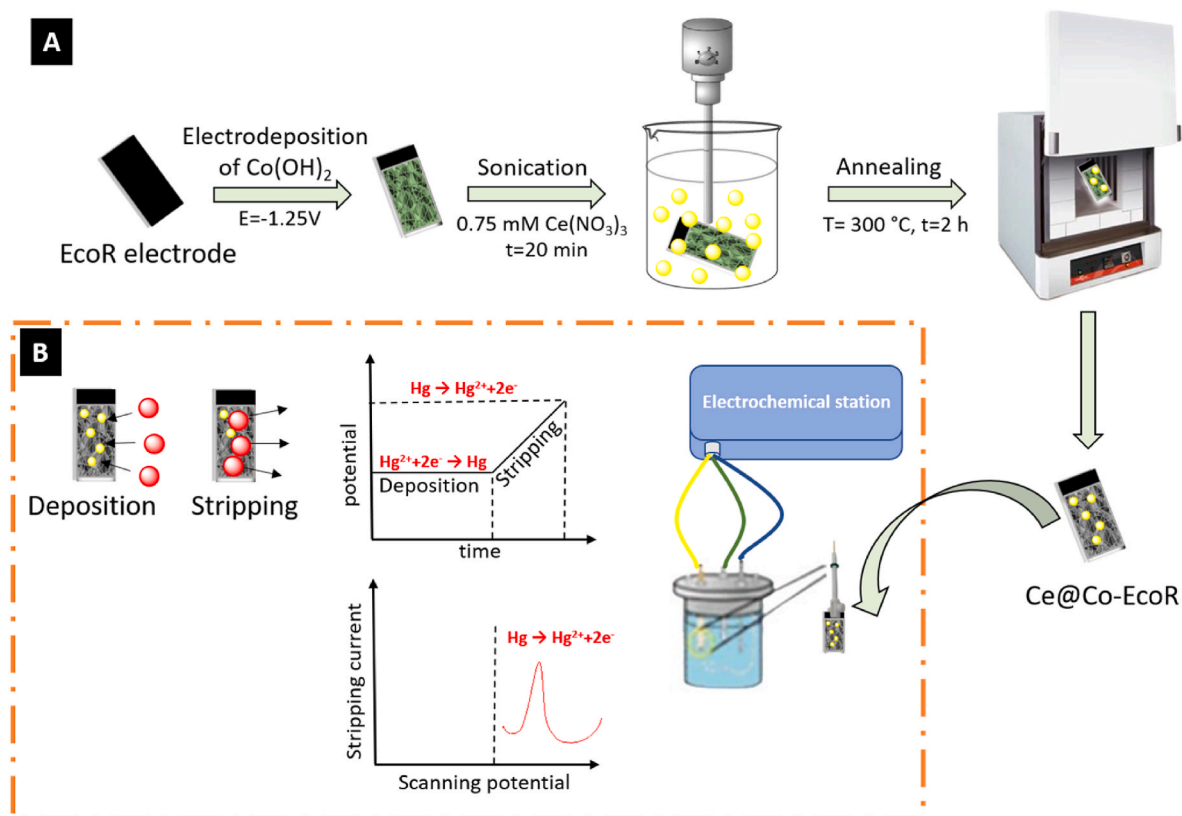


Fig. 1. (A) Fabrication process of the electrochemical sensor for Hg(II) and (B) SWSV analysis with the proposed Ce@Co-EcoR electrode.

Electrochemical impedance spectroscopy (EIS) was utilized to determine the resistance of the prepared electrode. The working electrode was immersed in a solution of  $5 \text{ mM K}_3\text{Fe}(\text{CN})_6/\text{K}_4\text{Fe}(\text{CN})_6$  with  $0.1 \text{ M KCl}$ , and measurements were taken across a frequency band of  $0.1\text{--}100 \text{ KHz}$  at  $0.2 \text{ V}$ . Cyclic voltammetry measurements were conducted using a same solution.

## 2.5. Mercury detection

The electrochemical detection of mercury using the proposed Ce@Co-EcoR sensor was performed through SWSV measurements. Mercury was electrochemically deposited on the working electrode under specific conditions: a deposition time of  $240 \text{ s}$  and a deposition potential of  $-1.0 \text{ V}$  (vs.  $\text{Ag}/\text{AgCl}$ ), within a phosphate buffer solution at a pH of  $5.0$  (Fig. 1 (B)). Following this, the reduced form was anodically

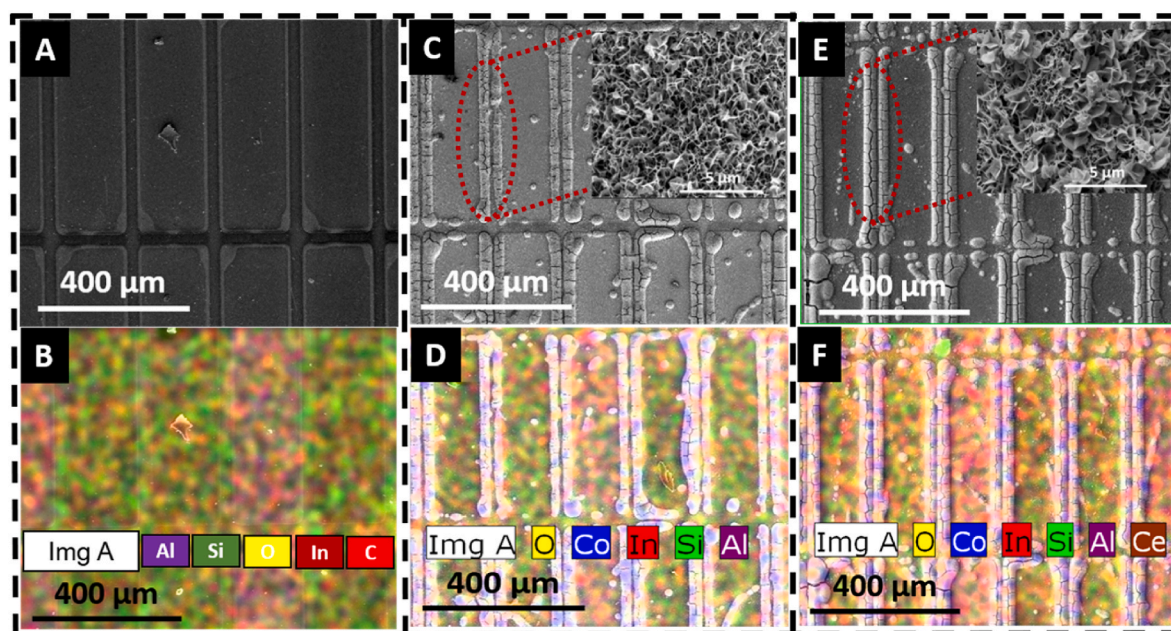


Fig. 2. SEM images of EcoR (A), Co-EcoR (C), Ce@Co-EcoR (E) and their corresponding elemental mappings (B, D, F), respectively.

stripped using a voltage that varied between  $-0.1$  to  $0.7$  V. The procedure incorporated a pulse amplitude of  $25$  mV, a frequency of  $25$  Hz, and a step amplitude of  $2$  mV.

### 3. Results and discussion

#### 3.1. Morphology and structure characterization

The surface morphology of both bare EcoR and modified EcoR samples was investigated using SEM and energy-dispersive X-ray spectroscopy (EDS-mapping), as shown in Fig. 2. The comparison between the SEM images of the bare EcoR (Fig. 2A) and the post-modification EcoR (Fig. 2B) highlights the formation of distinct layers in the  $\text{Co}_3\text{O}_4$  sample, achieved through electrodeposition techniques. The EDS mapping of the bare EcoR electrode (Fig. 2B) indicates the existence of other elements such as C, O, Al, Si, and In, which originate from the commercial coating of the LCD. Notably, indium, known for its excellent conductive properties in the form of indium oxide, was found in significant amount (Fig. S1). When cobalt oxide was electrodeposited, it formed a denser layer in regions containing indium. In the inset of Fig. 2B, it is evident that the thin layers of  $\text{Co}_3\text{O}_4$  resemble desert-rose nanosheets positioned on the EcoR electrode, featuring porous structures with a diameter of approximately  $250$  nm, offering a substantial surface area.

Furthermore, Fig. 2E illustrates the integration of  $\text{CeO}_2$  on the nanosheet-structured  $\text{Co}_3\text{O}_4$ , evidenced by a change in image contrast [20], confirming the successful formation of  $\text{Ce@Co-EcoR}$ . The  $\text{Co}_3\text{O}_4$  nanosheets are more uniformly interconnected, while the  $\text{Ce-Co}_3\text{O}_4$  nanosheets are more aggregated with wrinkles [21], as shown in the inset of Fig. 2E, further confirms the effective incorporation of cerium on the cobalt oxide surface. The EDS-mapping demonstrates the successful and uniform formation of  $\text{Co}_3\text{O}_4$ , and  $\text{CeO}_2@\text{Co}_3\text{O}_4$ , as depicted in Fig. 2D and F, respectively. Specifically, Fig. 2S reveals the presence of oxygen ( $41.72\%$ ), cobalt ( $54.35\%$ ), and cerium ( $3.93\%$ ) elements, confirming the successful incorporation of cerium oxide into  $\text{Co}_3\text{O}_4$ .

The porous, free-standing structure of the modified-EcoR revealed

through TEM an ensemble of interconnected nanoparticles (Fig. 3A), each measuring approximately  $5$  nm in size. Fig. 3B shows lattices fringes measuring  $0.24$  nm was assigned to the  $(311)$  plane of  $\text{Co}_3\text{O}_4$  [22] and  $0.31$  nm was attributed to the  $(111)$  plane of  $\text{CeO}_2$  [21]. In Fig. 3C, the XRD patterns of  $\text{Ce@Co-EcoR}$  approve the presence of ceria nanoparticles on the modified-electrodes. This is evident from the appearance of the characteristic diffraction peaks at  $28.7^\circ$ ,  $33.5^\circ$ ,  $47.6^\circ$  and  $56.4^\circ$ , conforming to the crystal planes  $(1\ 1\ 1)$ ,  $(2\ 0\ 0)$ ,  $(2\ 2\ 0)$  and  $(3\ 1\ 1)$ , respectively [23]. Conversely, these peaks are absent in the XRD pattern of LCD modified with solely ceria. Therefore, this observation confirms that the porous structure of the cobalt nanosheets facilitate the intercalation of the ceria nanoparticles.

XPS was employed to identify the elemental composition and electronic states on the material surfaces. The XPS survey (Fig. 4A) revealed distinct peaks for C, O, Al, N, Si, and In, confirming the surface composition of EcoR (a component of the LCD). Additionally, the presence of peaks corresponding to Ce, Co, and O confirmed the successful modification to  $\text{Ce@Co-EcoR}$ . The high-resolution deconvoluted XPS spectra of Co 2p (Fig. 4B) showed three distinct parts: i) peaks at  $777.8$  and  $792.8$  eV attributed to  $\text{Co}^{2+}$ ; ii) peaks at  $779.2$  eV and  $794.3$  eV attributed to  $\text{Co}^{3+}$ ; and iii) their satellite peaks at  $785.1$  eV and  $803.2$  eV. The Ce 3d spectrum (Fig. 4C) displayed noticeable shakeup satellite peaks. The characteristic peaks of Ce  $3d_{3/2}$  and Ce  $3d_{5/2}$  were fitted in accordance with established references [24]. The presence of  $\text{CeO}_2$  was verified based on the binding energies of  $\text{Ce}3d_{5/2}$  and  $\text{Ce}3d_{3/2}$ , which were observed at  $880$ ,  $896.7$ ,  $899.6$ , and  $915$  eV. Additionally, two satellite peaks, denoted sat., appeared at  $887.7$  and  $905.4$  eV, respectively. Furthermore, the existence of  $\text{Ce}^{3+}$  ions was demonstrated by the appearance of two sub-bands at  $882.5$  and  $901.2$  eV [25,26]. The interaction between ceria and cobalt generally lead to shifts in the binding energies, indicating changes in oxidation states and electronic structure. This is supported by the observation that, following ceria insertion, the highest binding energy of Co 2p in  $\text{Ce@Co-EcoR}$  shifts by approximately  $1.7$  eV towards higher binding energy (Fig. 4A) [27]. Fig. 4 (D, E) displays the photoelectron peaks of O 1s for the Co-EcoR and  $\text{Ce@Co-EcoR}$  electrodes. The O 1s spectrum revealed the presence

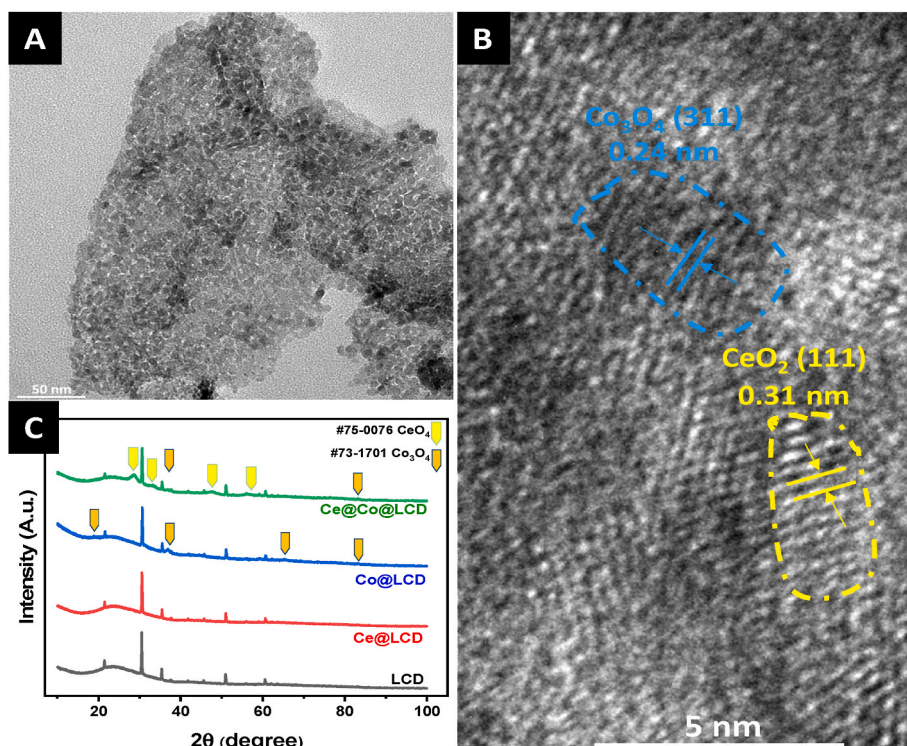
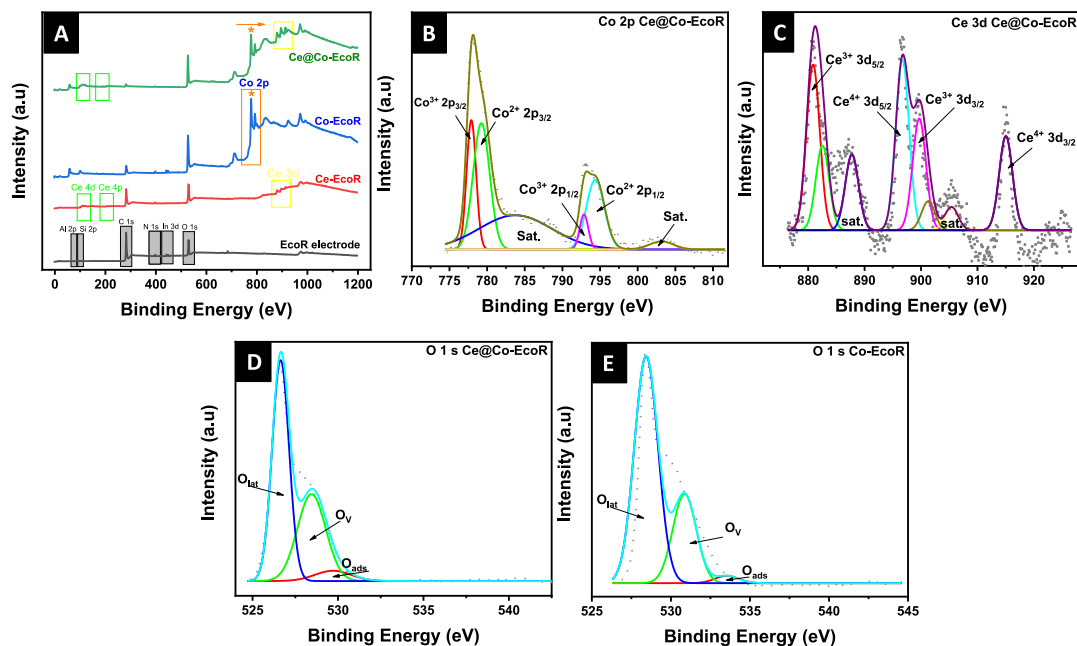


Fig. 3. (A–B) TEM of  $\text{CeO}_2@\text{Co-EcoR}$  and (C) XRD pattern of EcoR, Ce-EcoR, Co-EcoR,  $\text{Ce@Co-EcoR}$ .



**Fig. 4.** (A) An XPS scan for different electrodes, high-resolution spectra were acquired for the (B) Co 2p and, (C) Ce 3d, (D) O 1s of the Ce@Co-EcoR and (E) O 1s of the Co-EcoR.

of three distinct peaks for both electrodes: the lattice oxygen peak (528.4 eV, 526.6 eV), the oxygen vacancy peak (530.8 eV, 528.4 eV), and the adsorbed oxygen peak (533.5 eV, 529.7 eV), respectively. Moreover, Ce@Co-EcoR exhibited a higher concentration of oxygen vacancies compared to Co-EcoR, indicated by the peak area ratio of oxygen vacancies: 37.4% for Ce@Co-EcoR versus 27.5% for Co-EcoR.

### 3.2. Electrochemical characterization of the Ce@Co-EcoR electrode

To evaluate the efficacy of the modified electrode, EIS and CV were employed. EIS provided crucial information about the transformations occurring on the electrode surface. These insights were particularly valuable during the modification process. In Fig. 5A, EIS Nyquist plots of GCE (a), bare EcoR (extracted part of LCD) (b), and Ce@Co-EcoR (c) electrodes, are presented in the presence of 5 mM of  $[\text{Fe}(\text{CN})_6]^{3/4-}$  as a redox probe. The Faradaic EIS of both GCE and EcoR electrodes exhibited a similar shape characterized by the equivalent circuit R(QR) (Fig. 5A (a,b)), with a noticeable decrease in transfer resistance of the EcoR electrode. This diminution was evidenced by the LCD electrode

displaying the smallest diameter of the semicircle portion in the Nyquist plots, which provides information about the charge-transfer resistance ( $R_{CT} = 2644 \Omega \text{ cm}^{-2}$ ). On the other hand, the GCE electrode had an  $R_{CT}$  value of ( $R_{CT} = 5297 \Omega \text{ cm}^{-2}$ ). Upon modification of the EcoR with Ce@Co nanomaterials, the shape of the circle changed to reveal two semicircles and an appropriate equivalent circuit was well modeled by a Voigt type R(QR)(QR) containing two capacitive loops Fig. 5A (c), with the  $R_{CT}$  value dropping to ( $R_{CT} = 1042 \Omega \text{ cm}^{-2}$ ). The significant reduction in transfer resistance demonstrated that the modified electrode displayed enhanced electron-transfer kinetics. In Fig. 5A, the electrolyte resistance is indicated by  $R_s$  while the constant phase element (CPE) and resistance of the porous modified electrode are represented by  $Q_c$  and  $R_c$  respectively. Similarly,  $Q_{dl}$  and  $R_{ct}$  correspond to the constant phase element and resistance of the interface between electrolyte resistance and the electrode. The constant phase element, was strategically employed in the circuit as an alternative to the pure double-layer capacitor. This substitution was performed to accurately model the electrode surface, which exhibited inherent heterogeneity due to factors such as surface roughness, dislocations, impurities,

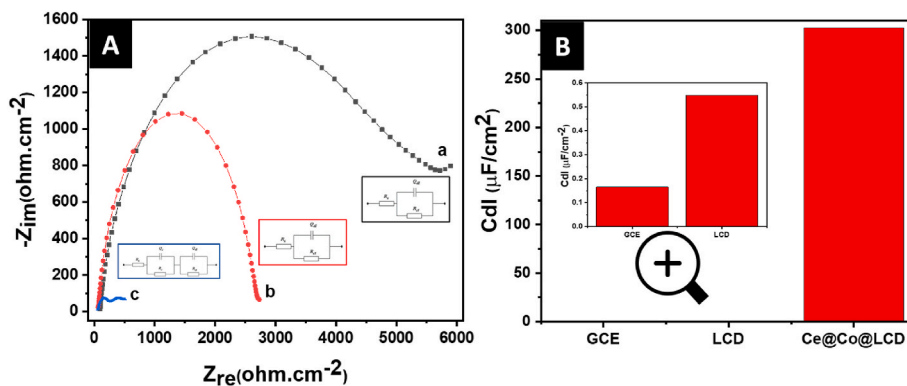


**Fig. 5.** (A) EIS plots obtained from bare GCE (a), LCD (b) and Ce@Co-EcoR (c) in a KCl (0.1 M) solution with 5 mM  $[\text{Fe}(\text{CN})_6]^{3/4-}$  as a redox probe and (B) The double-layer capacitance histogram.

inhibitor adsorption, grain boundaries, and the formation of porous layers [28,29]. By integrating the CPE into the circuit, a more accurate fit [30] was achieved, allowing a comprehensive understanding of impedance dynamics. The impedance of the CPE can be described by the following expression:

$$Z_{CPE} = Y_{dl}^{-1} (i\omega)^{-n} \quad (1)$$

In this context,  $Y_{dl}$  represents the magnitude of the constant phase element (CPE) (in  $\Omega^{-1} s^n cm^{-2}$ ),  $\omega$  indicates the angular frequency of the sine wave modulation (in  $rad s^{-1}$ ),  $i_2 = -1$  denotes the imaginary unit, and  $n$  is an empirical exponent ranging from 0 to 1, which measures the deviation from ideal capacitive behavior [31,32]. The fitting results are provided in Table 1. Fig. 5B presents the calculated double-layer capacitance ( $C_{dl}$ ), which is derived from the CPE parameters and obtained using the equation below [33]:

$$C_{dl} = \frac{(Y_{dl} R_{ct})_{ndl}^{-1}}{R_{ct}} \quad (2)$$

Furthermore, the electrochemically active surface area (ECSA) of the Ce@Co-EcoR was estimated through double-layer capacitance ( $C_{dl}$ ) using the EIS technique, as defined by the following expression:

$$ECSA = S \frac{C_{dl}}{22 \mu F \cdot cm^{-2}} \quad (3)$$

Here,  $S$  represents the geometric surface area of the thin films (approximately  $1 cm^2$ ). The electrochemical surface area (ECSA) of Ce@Co-EcoR was determined to be  $13.75 cm^2$ .

Fig. 6A visually demonstrates the superior electron-transfer kinetics of the electrode, further confirmed by CV. The analysis revealed that Ce@Co-EcoR exhibited a smaller potential difference between its peak points and a higher maximum current value compared to the bare electrodes. This improvement is credited to the remarkable conductivity and extensive porosity of the modifying material, which facilitates easier diffusion of the redox probe to the electrode surface due to its large electroactive surface area.

The electrochemically active surface area (ECSA) of the Ce@Co-EcoR sensing platform was also determined using the Randles Sevcik equation [34].

$$I_p = 2.69 \times 10^5 A C n^{3/2} D^{1/2} v^{1/2} \quad (4)$$

where  $I_p$  is the peak current density ( $A \cdot cm^{-2}$ ),  $n = 1$  corresponds to the number of electrons involved in the redox reaction,  $A$  denoted the electroactive area ( $cm^2$ ),  $C$  designates the molar concentration of the probe molecule,  $D$  refers to the diffusion coefficient of probe molecule ( $cm^2 \cdot s^{-1}$ ) and  $v$  represents the scan rate ( $V \cdot s^{-1}$ ).

Cyclic voltammetry was conducted at various scan rates (as depicted in Fig. 6B). Utilizing the diffusion constant of  $7.6 \times 10^{-6} cm^2 s^{-1}$  of  $[Fe(CN)_6]^{3/4-}$ , the electrochemical surface area (ECSA) was calculated to be  $12 cm^2$  from the slope of the linear plot of  $I_p$  versus  $v$ .

### 3.3. Influence of the operation parameters on mercury detection

#### 3.3.1. Electrode modification effects on the mercury sensing

To verify the feasibility of the Ce@Co-EcoR sensing electrode for Hg (II), a series of SWSV were carried out in phosphate buffer solution (PBS). Square-wave stripping voltammetry (SWSV) was chosen for electrochemical testing due to its distinct advantages, like rapid analysis

with high sensitivity [35] particularly in a heavy metals detection [36]. While differential pulse voltammetry (DPV) was also widely recognized as the most sensitive method [37,38], but as comparable to SWSV. It provides high sensitivity with the additional advantage of faster analysis, and unaffected by dissolved oxygen, as a common interference which makes it ideal for quantitative analytical applications [39].

As shown in Fig. 7, when the unmodified EcoR electrode (Fig. 7a) was used to detect mercury, a peak appeared at 0.15V with the lowest current density. However, after modifying the EcoR electrode with cobalt oxide (Fig. 7b), the peak position remained unchanged, but the current density increased significantly. This improvement is attributed to the catalytic effect of cobalt oxide, which enhances the electrodeposition of Hg(II) by increasing the electrode's surface area and generating oxygen vacancies in the oxide structure. To further enhance sensitivity, the Co/EcoR electrode was modified with cerium oxide (Fig. 7c), which resulted in an even higher current density due to the additional oxygen vacancies created on the electrode surface, further improving the electrode's performance for mercury detection.

#### 3.3.2. Time and potential effects of cobalt oxide nanosheet electrodeposition

To further improve the Ce@Co-EcoR -based sensor performances, the impact of electrodeposition potential and duration on the formation of cobalt oxide nanosheets was investigated. One potential was tested along with different durations of the cobalt oxide deposition. The electrodes were maintained at  $-1.25V$ , by reducing potential of cobalt nitrate. It was observed that the highest detection currents of Hg(II) were achieved at 6 min. Interestingly, when the deposition time exceeds this value dense layers of cobalt oxides were formed, while the mercury detection capabilities were not improved (Fig. 8). These thick coatings might slow down the speed at which electrons transfer at the electrode-to-electrolyte interface [40].

#### 3.3.3. The influence of pH, mercury deposition potential and time on electrode activity

The influence of pH on the response of the modified electrode was further studied in a phosphate buffer solution with a pH spanning in the range between 2.0 and 6.0. The extracted data is displayed in Fig. 9A. The amperometric response reached its optimal value at  $pH = 5.0$  because mercury existed as  $Hg^{2+}$  in acidic pH. However, if the pH was lower than this value, higher  $H^+$  concentration led to hydrogen generation during of electroreduction process. This could occupy active sites on the electrode surface by bubbles. Moreover, hydrogen evolution reaction would compete with the reduction of  $Hg^{2+}$ , thereby influencing the preconcentration of  $Hg^{2+}$  and diminishing the resulting current. Conversely, in basic pH solution, it precipitated out as insoluble Hg (OH)<sub>2</sub>. Similarly, the E-pH diagram reveals that the electrode does not follow a clear linear trend across various pH values, indicating that  $H^+$  or  $OH^-$  ions are not significantly involved in the reaction.

The optimal working potential of the sensor corresponds to the maximum of the oxidation current produced by the deposited mercury. A sequence of prospective experiments was conducted to achieve an optimal equilibrium between the generated electric current and the operational potential. Fig. 9B exposes the histogram plotting the current vs. the applied potential for fixed amount of mercury (0.3 ppm). The data prove that a potential of  $-1.0 V$  vs. AgCl/Ag represents a favorable compromise between the mercury addition and the current density, since it generates enough current to detect of mercury.

It can be noticed that, at the optimal deposition potential ( $-1.0 V$ ), the performance of the electrode raises with the increase of the deposition time until reaching 240 s (Fig. 9C).

### 3.4. Sensor metrics

#### 3.4.1. Quantitative analysis of mercury

The newly designed Ce@Co-EcoR-based sensor was used under

**Table 1**

Impedance parameters of the different electrodes.

Electrodes	$Y_{dl}$ ( $\mu F \cdot cm^{-2}$ )	$n_{dl}$	$R_{ct}$ ( $\Omega \cdot cm^2$ )
GCE	5.2	0.52	4599
EcoR	11.26	0.89	2646
Ce@Co- EcoR	1020	0.3371	527.7

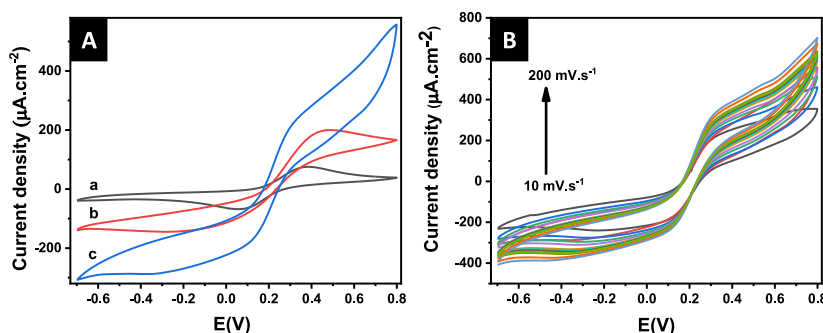


Fig. 6. (A) CV curves obtained from bare GCE (a), EcoR (b) and Ce/Co/EcoR (c) in KCl (0.1 M) solution with a 5 mM of  $[\text{Fe}(\text{CN})_6]^{3/4-}$  as a redox probe and (B) CV curves of the Ce@Co-EcoR at various scan rates.

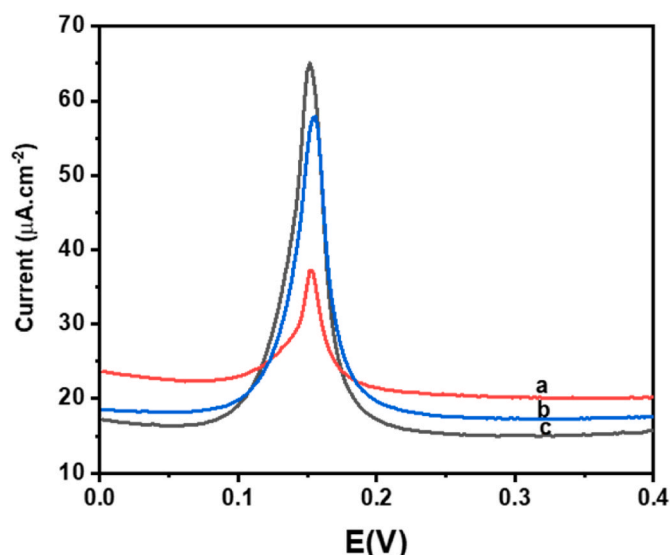


Fig. 7. SWSVs of the bare EcoR (a), Co/EcoR (b) and Ce@Co-EcoR (c) in a 0.1 M phosphate buffer (pH 5.0) solution containing Hg(II).

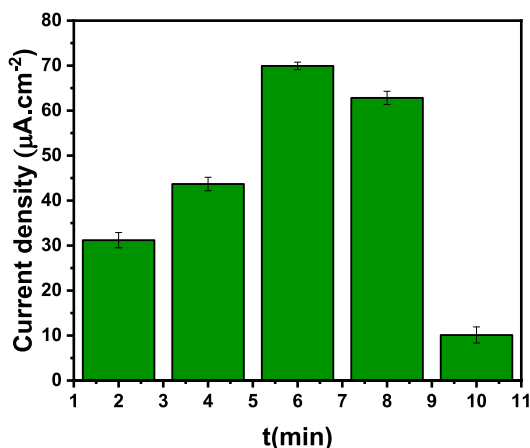


Fig. 8. Influence of Cobalt Oxide coating duration on the performance of Mercury sensor in 0.3 ppm Hg(II) solution.

optimum circumstances for the electroanalytical monitoring of  $\text{Hg}^{2+}$  ions. As shown in Fig. 10A, the SWSV voltammograms for mercuric ions indicate a progressive increase in the stripping peak current response with higher concentrations of  $\text{Hg}^{2+}$ . The current-concentration relationship demonstrates a linear rise in peak current as the Hg(II) concentration increases, following the linear equation  $Y (\mu\text{A}.\text{cm}^{-2}) = 22.37 + 158.28X (\text{ppm})$  with  $R^2 = 0.993$  (Fig. 10B). The sensor shows quite a dynamic range of response comprised between 16 and 620 ppb with high sensitivity estimated at  $158.28 \mu\text{A}.\text{cm}^{-2} \text{ppm}^{-1}$ . This is likely due to two factors: the large surface area of the working electrode and the stable existence of various oxidation states for both ( $\text{Ce}^{3+}/\text{Ce}^{4+}$ ) and ( $\text{Co}^{2+}/\text{Co}^{3+}$ ). These features improve the sensor's electrical properties, enabling effective electron transfer from the target substance to the redox-active electrode.

The limit of detection (LOD) was determined using Equation (5), which involves multiplying the standard deviation of the blank signal ( $s_b$ ) by three and dividing it by the response sensitivity (S). Similarly, the limit of quantification (LOQ) for the lower concentration range was determined by multiplying the standard deviation of the blank signal by ten and then dividing by the response sensitivity [41].

$$\text{LOD}(Q) = (n \times s_b) / S \quad (5)$$

where  $n = 3$  (D) or 10 (Q). The calculated limits of detection and quantification of the sensor were equal to 2.8 ppb and 9.6 ppb, respectively. They complied with the allowable limits established by the US EPA for heavy metal ions in a drinking water.

### 3.4.2. Adsorption mechanism explored by XPS

In order to delve deeper into the adsorption mechanism of Hg(II) on the modified electrode, XPS was utilized to analyze the structural alterations of Ce@Co-EcoR following Hg(II) adsorption. Notably, the survey-scan (Fig. 11A) showed a new binding energy peak at 101.5 eV attributed to Hg4f photoelectron and signifying the adsorption of Hg(II) onto Ce@Co-EcoR. Deconvolution of the Hg 4f spectrum (Fig. 11B) reveals two peaks at 100.8 and 104.9 eV, indicating Hg(II) adsorption. This equates to a spin-orbit separation of 4.1 eV for the  $4f_{5/2}$  and  $4f_{7/2}$  levels, respectively [42]. Additionally, the analysis of Co 2p and Ce 3d spectrum after Hg(II) adsorption reveals a shift toward the positive energy, suggesting an electron-deficient state (Fig. 11C,D). Also, the XPS O 1s spectrum of Ce@Co-EcoR demonstrates a downward shift in the OV and  $\text{O}_{\text{lat}}$  peaks, probably because of the electron gain during the adsorption reaction.

### 3.5. Validation experiments

To validate the analytical method, experiments were conducted to assess interference, stability and reproducibility. The effectiveness of the electrochemical sensors was evaluated based on their ability to resist the

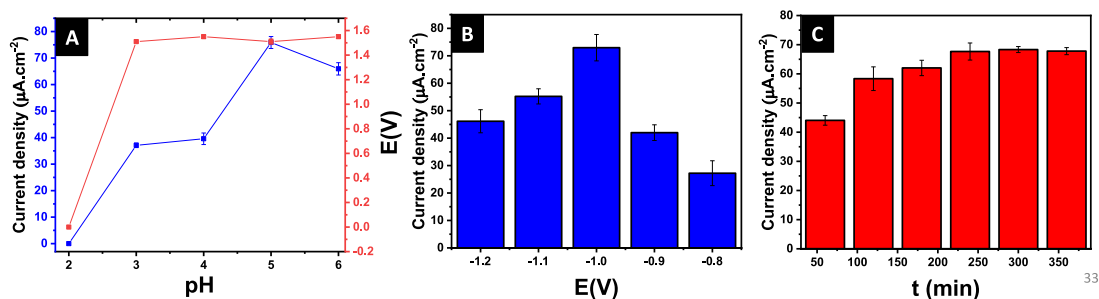


Fig. 9. (A) Effect of optimized pH, (B) depositing potential and (C) depositing time on Ce@Co-EcoR based sensor performance using 0.3 ppm of Hg(II) solution.

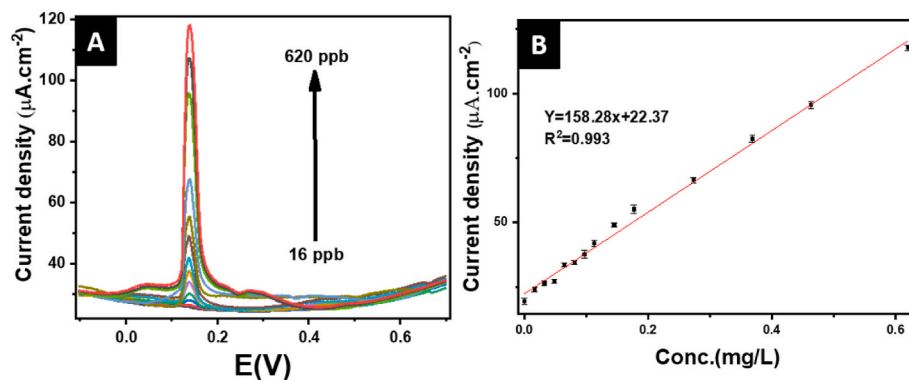


Fig. 10. (A) SWSVs of the sensor in a 0.1 M phosphate buffer (pH 5.0) solution containing various amount of  $\text{Hg}^{2+}$ , (B) The correlation between the oxidation peak current and  $\text{Hg}^{2+}$  amount, with a recorded RSD of around 1.5% ( $n = 3$ ).

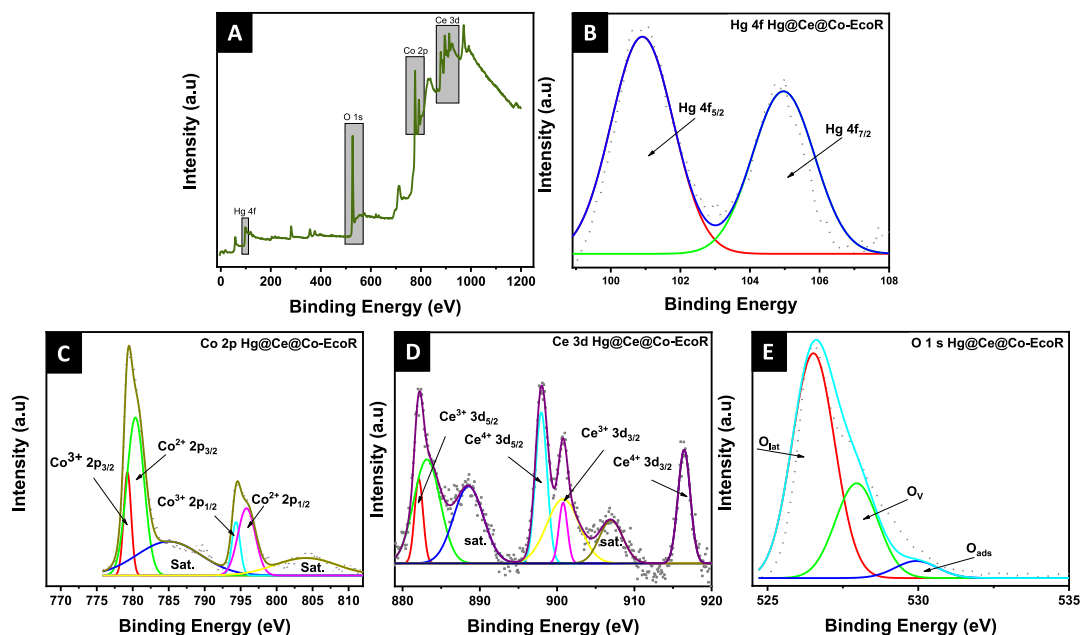
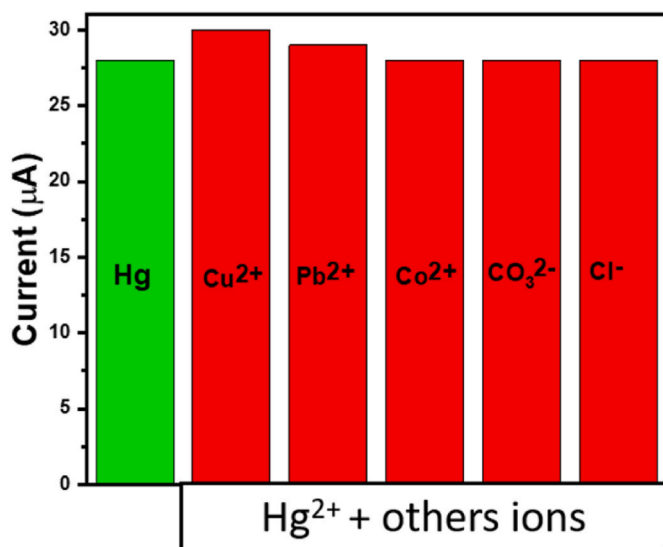


Fig. 11. (A) XPS survey of Ce@Co-EcoR after adsorption of Hg(II) and high-resolution after Hg(III) adsorption of (B) Hg 4f, (C) Co 2p, (D) Ce 3d and (E) O 1s of the Hg@Ce@Co-EcoR.

interference. The activity of the modified electrode towards mercury was further tested by current-time response (Fig. 3S) for potential interference from ions such as copper, lead, cobalt, carbonate, and chloride, all at physiological concentrations (1  $\mu\text{M}$ ) typically found in

real-world samples. The histogram presented in Fig. 12 reveals that the addition of mercury led to a noticeable increase in current density. This also shows that the addition of other ions did not cause any significant increase in current, highlighting the sensor's high anti-jamming ability.



**Fig. 12.** Histogram illustrating the variation in current value of the Ce@Co-EcoR sensor in response to 0.1  $\mu\text{M}$  Hg(II) amid 1  $\mu\text{M}$  concentrations of Cu(II), Pb(II), Co(II),  $\text{CO}_3^{2-}$ , and  $\text{Cl}^-$ .

The repeatability and stability tests of the sensor were conducted by recording the current density response of 5 different modified-electrodes over a five-weeks period (Fig. 13A). The sensor's exceptional repeatability was demonstrated by the relative standard deviation (RSD) of five repeated readings, which was 3%, well below the 5% threshold. Additionally, the modified-EcoR electrode maintained over 80% retention, indicating their exceptional stability. Moreover, Fig. 13B demonstrate reproducibility of the developed Ce@Co-EcoR electrode, which evaluated by using three identical parallel electrodes. These electrodes were prepared separately and subjected to the same experimental conditions. Through SWSV method it shows the maximum gap in current density was observed  $0.332 \mu\text{A}/\text{cm}^2$ .

### 3.6. Electro-analysis for sea water sample

The proposed method was assessed for its analytical reliability and practical applicability by employing an electrochemical sensor to detect mercury in aquatic environments. Specifically, real water sample were collected from Al Wakra sea, in Qatar. Prior testing, the sea water was filtered and used directly, without dilution or any additional treatment. Afterwards, the standard  $\text{Hg}^{2+}$  was introduced to the solution and analyzed via SWSV (Fig. 14). The SWSV spectra revealed that the oxidation peak increased linearly by adding the mercury, showing a good linearity. Sensitivity equal to  $864.22 \mu\text{A}/\text{cm}^2 \text{ ppm}^{-1}$  was

determined from the linear fitting curve, demonstrating 5 times the sensitivity compared to that obtained using the phosphate buffer solution (pH 5). This ratio reflects the difference between the conductivity of the sea water and PBS mediums. Subsequent calculation of recovery (Table 2), based on two concentration of Hg(II) (0.016, 0.090 and 0.113 ppm), yielded a 100%, 89% and 97%, respectively. Generally, the accepted range for recovery falls between 80% and 120% [43]. This finding validates the applicability of the proposed sensor.

### 3.7. Comparison with literature

The as-prepared sensor, developed using an eco-recycled electrode, was compared with others electrochemical sensors based on commercial electrodes from previous studies. Table 3, summarizing the collected data, indicates that the Ce@Co-EcoR-based sensor possesses exceptional electrochemical characteristics, making it a viable option for the ultra-sensitive detection of  $\text{Hg}^{2+}$  in undiluted and unaltered pH sea water.

## 4. Conclusion

This study concludes by emphasizing the groundbreaking invention and first-time application of an electrochemical sensor based on an LCD for the precise measurement of  $\text{Hg}^{2+}$  ions in seawater. The sensor, featuring a ceria/cobalt nanocomposite deposited on a modified EcoR, exhibited a remarkable performance. The Ce@Co-EcoR sensor exhibited an excellent linear detection range from 16 to 620 ppb, a trace-level detection limit of around  $\sim 3$  ppb, and high sensitivity of  $158.28 \mu\text{A}/\text{ppm}^{-1}\text{cm}^{-2}$  for  $\text{Hg}^{2+}$  detection. The electrochemical measurements demonstrated that the Ce@Co-EcoR sensor exhibits outstanding anti-interference performance, effectively withstanding various common interferents. The proposed EcoRelectrode for mercury sensing shows great potential for  $\text{Hg}^{2+}$  detection in real-time environmental monitoring. It demonstrated robust analytical reliability, reproducibility, and stability, highlighting its suitability for practical use. This innovative sensor paves the way for advancements in heavy metal detection technologies.

### CRediT authorship contribution statement

**Maroua Saadaoui:** Writing – original draft, Visualization, Methodology, Investigation, Formal analysis. **Assem T. Mohamed:** Investigation, Data curation. **Abdul Hakeem Anwer:** Writing – original draft, Formal analysis, Data curation. **Siham Y. Al-Qaradawi:** Validation, Resources, Conceptualization. **Mazen Khaled:** Formal analysis, Conceptualization. **Abdelbaki Benamor:** Writing – review & editing, Validation, Supervision, Project administration, Conceptualization.

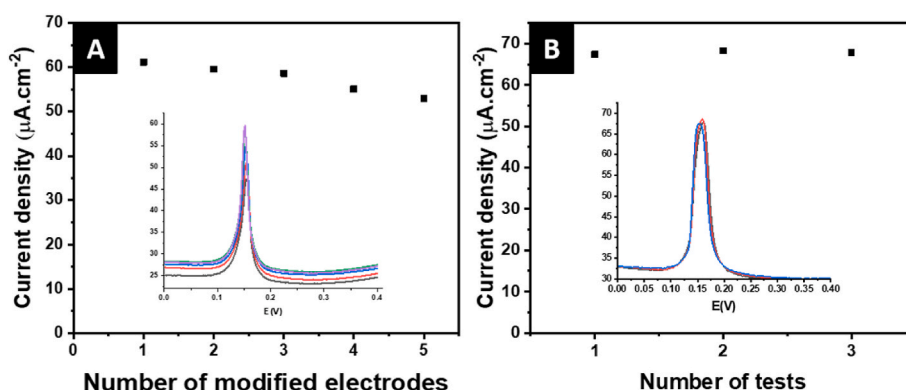


**Fig. 13.** (A) Repeatability and stability tests, (B) reproducibility test of the Ce@Co-EcoR towards Hg(II).

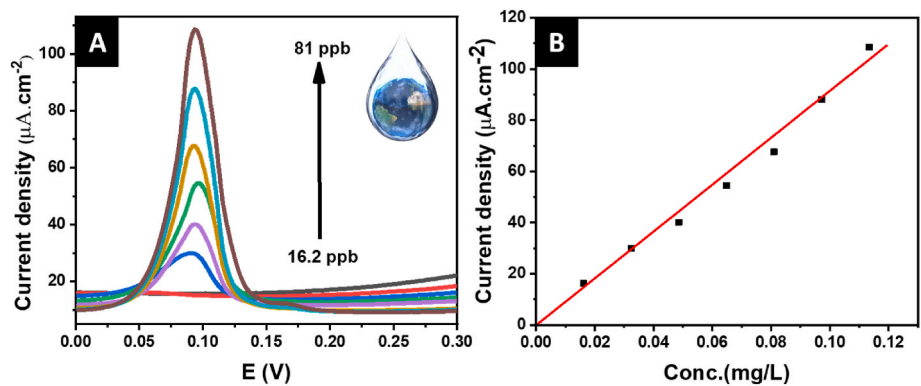


Fig. 14. (A) SWSVs registered in sea water with increasing concentration of Hg(II), (B) the linear fitting curve of the Ce@Co-EcoR sensor.

**Table 2**  
Application of sensor to determine of Hg (II) levels in sea water.

Sample	Detected (mg/L) (P)	Added (mg/L) (Q)	Found (mg/L) (R)	Recovery % ± RSD (%; n = 3) (R–P/Q)*100
Sea water	0	–	ND	–
	0	0.016	0.016	100 ± 2.59
	0	0.090	0.080	89 ± 2.35
	0	0.113	0.110	97 ± 4.57

ND: Not detected.

**Table 3**  
Summary of studies introducing mercury sensing devices utilizing various electrode modification materials with SWSV is used as the principal investigation technique.

Sensors	Linear range/μM	LOD/μM	Real-Time sample	Refs.
Ni-doped Co <sub>3</sub> O <sub>4</sub> /GCE	0–1.6	0.009	Lake/tap water	[44]
Alk-Ti <sub>3</sub> C <sub>2</sub> /GCE	1.0–1.9	0.066	–	[45]
Pd NPs/porous activated carbons/GCE	0.24–7.5	0.027	Milk	[46]
TiO <sub>2</sub> /GCE	0.1–2.3	0.017	–	[47]
Ce–Zr oxide/GCE	0.02–0.5	0.006	Waste water	[48]
CNFs/AuNPs/SPCE	0.1–1.2	0.03	River water	[49]
Ru/CeO <sub>2</sub> nanocomposites	0.04–0.8	0.019	Tap water	[50]
NaPb <sub>4–x</sub> Cd <sub>x</sub> (PO <sub>4</sub> ) <sub>3</sub> /CE	0.9–100	0.0135	Sea water	[51]
Ce@Co-EcoR	0.049–1.9	0.008	Sea water	<b>This work</b>

**Note:** GCE: glassy carbon electrode; CE: carbon electrode; SPCE: screen printed carbon electrode; NPs: nanoparticles; CNFs: Carbon nanofibers; Au: gold nanoparticles; Ru: ruthenium; NaPb<sub>4–x</sub>Cd<sub>x</sub>(PO<sub>4</sub>)<sub>3</sub>: lacunar apatite.

**Declaration of competing interest**

The authors declare that they have no known competing financial interests or personal relationships that could have appeared to influence the work reported in this paper.

**Acknowledgements**

This work possible through Qatar University internal grant # IRCC 2024-003. The SEM analysis was accomplished in the Central Laboratories unit, Qatar University.

**Appendix A. Supplementary data**

Supplementary data to this article can be found online at <https://doi.org/10.1016/j.mtsust.2024.101015>.

**Data availability**

Data will be made available on request.

**References**

[1] V. Singh, G. Ahmed, S. Vedika, P. Kumar, S.K. Chaturvedi, S.N. Rai, E. Vamanu, A. Kumar, Toxic heavy metal ions contamination in water and their sustainable reduction by eco-friendly methods: isotherms, thermodynamics and kinetics study, *Sci. Rep.* 14 (2024) 7595.

[2] F. Xie, M. Yang, Z.-Y. Song, W.-C. Duan, X.-J. Huang, S.-H. Chen, P.-H. Li, X.-Y. Xiao, W.-Q. Liu, P.-H. Xie, Highly sensitive electrochemical detection of Hg(II) promoted by oxygen vacancies of plasma-treated ZnO: XPS and DFT calculation analysis, *Electrochim. Acta* 426 (2022) 140757.

[3] L.N. Suvarapu, S.-O. Baek, Determination of heavy metals in the ambient atmosphere: a review, *Toxicol. Ind. Health* 33 (2017) 79–96.

[4] P.F. Schuster, K.M. Schaefer, G.R. Aiken, R.C. Antweiler, J.F. Dewild, J.D. Gryziec, A. Gusmeroli, G.P. Hugelius, E. Jafarov, D.P. Krabbenhoft, L. Liu, N. Herman-Mercer, C. Mu, D.A. Roth, T. Schaefer, R.G. Striegl, K.P. Wickland, T. Zhang, Permafrost stores a globally significant amount of mercury, *World Scientific Encyclopedia of Climate Change* (2021) 155–164. World Scientific.

[5] M. Jaishankar, T. Tseten, N. Anbalagan, B.B. Mathew, K.N. Beeregowda, Toxicity, mechanism and health effects of some heavy metals, *Interdiscipl. Toxicol.* 7 (2014) 60–72.

[6] B. Amanulla, K.N. Perumal, S.K. Ramaraj, Chitosan functionalized gold nanoparticles assembled on sulphur doped graphitic carbon nitride as a new platform for colorimetric detection of trace Hg<sup>2+</sup>, *Sensor. Actuator. B Chem.* 281 (2019) 281–287.

[7] G. Aragay, J. Pons, A. Merkoçi, Recent trends in macro-, micro-, and nanomaterial-based tools and strategies for heavy-metal detection, *Chemical reviews* 111 (2011) 3433–3458.

[8] L. Andeobu, S. Wibowo, S. Grandhi, An assessment of e-waste generation and environmental management of selected countries in Africa, Europe and North America: a systematic review, *Sci. Total Environ.* 792 (2021) 148078.

[9] V. Savvilitidou, J.N. Hahladakis, E. Gidarakos, Determination of toxic metals in discarded liquid crystal displays (LCDs), *Resour. Conserv. Recycl.* 92 (2014) 108–115.

[10] P.V. Vaishag, S.A. Mohandas, M. Mufeeda, P. Gangadharan, P.A. Rasheed, Conversion of electronic waste to an electrochemical sensor for dopamine: using MXene-modified liquid crystal display panels, *ACS Sustain. Chem. Eng.* 11 (2023) 12771–12779.

[11] J. Zhang, Q. Xiong, J. Xu, Research progress in non-precious metal oxide/compound-based electrodes for non-enzymatic electrochemical glucose sensor applications, *Mater. Sci. Semicond. Process.* 181 (2024) 108643.

[12] X. Hu, L. Wei, R. Chen, Q. Wu, J. Li, Reviews and perspectives of Co3O4-based nanomaterials for supercapacitor application, *ChemistrySelect* 5 (2020) 5268–5288.

[13] S. Li, X. Ma, C. Pang, M. Wang, G. Yin, Z. Xu, J. Li, J. Luo, Novel chloramphenicol sensor based on aggregation-induced electrochemiluminescence and nanozyme amplification, *Biosens. Bioelectron.* 176 (2021) 112944.

[14] Z. Hao, J. Lyu, M. Tian, X. Zhang, K. Wang, S.-W. Yang, Y. Zhang, G.Q. Xu, Unraveling the synergistic effects of oxygen vacancy and amorphous structure on TiO<sub>2</sub> for high-performance lithium storage, *Small Structures* 5 (2024) 2300442.

[15] S. Parwaiz, K. Bhunia, A.K. Das, M.M. Khan, D. Pradhan, Cobalt-doped ceria/reduced graphene oxide nanocomposite as an efficient oxygen reduction reaction catalyst and supercapacitor material, *J. Phys. Chem. C* 121 (2017) 20165–20176.

[16] L. Jiang, M. Yao, B. Liu, Q. Li, R. Liu, H. Lv, S. Lu, C. Gong, B. Zou, T. Cui, Controlled synthesis of CeO<sub>2</sub>/graphene nanocomposites with highly enhanced optical and catalytic properties, *J. Phys. Chem. C* 116 (2012) 11741–11745.

[17] X. Qi, Z. Wang, Graphene quantum dots functionalized Ce-ZnO nanofibers with enriched oxygen vacancy sites morphology to improve the efficiency of selective electrochemical detection of Hg (II), *Diam. Relat. Mater.* 139 (2023) 110241.

- [18] Q.-Q. Xu, X.-L. Cheng, B.-Y. Zhang, F. Zhang, X. Wang, S.-S. Li, Y.-X. Zhang, Fe-doping induced surface Fe<sup>2+</sup>/Fe<sup>3+</sup> cycle and activated redox-inert TiO<sub>2</sub> for enhanced Hg(II) electrochemical sensing: an efficient strategy to strengthen the redox activity, *Anal. Chim. Acta* 1232 (2022) 340472.
- [19] Q.T. Nguyen, U.T. Nakate, J. Chen, S. Park, S. Park, Ceria nanoflowers decorated Co<sub>3</sub>O<sub>4</sub> nanosheets electrodes for highly efficient electrochemical supercapacitors, *Appl. Surf. Sci.* 613 (2023) 156034.
- [20] Z.L. Wang, Transmission electron microscopy of shape-controlled nanocrystals and their assemblies, *J. Phys. Chem. B* 104 (2000) 1153–1175.
- [21] J. Huang, H. Sheng, R.D. Ross, J. Han, X. Wang, B. Song, S. Jin, Modifying redox properties and local bonding of Co<sub>3</sub>O<sub>4</sub> by CeO<sub>2</sub> enhances oxygen evolution catalysis in acid, *Nat. Commun.* 12 (2021) 3036.
- [22] X.-Y. Yu, Q.-Q. Meng, T. Luo, Y. Jia, B. Sun, Q.-X. Li, J.-H. Liu, X.-J. Huang, Facet-dependent electrochemical properties of Co<sub>3</sub>O<sub>4</sub> nanocrystals toward heavy metal ions, *Sci. Rep.* 3 (2013) 2886.
- [23] B. Xu, Q. Zhang, S. Yuan, M. Zhang, T. Ohno, Synthesis and photocatalytic performance of yttrium-doped CeO<sub>2</sub> with a porous broom-like hierarchical structure, *Appl. Catal. B Environ.* 183 (2016) 361–370.
- [24] S. Arunpandiyar, S. Vinoth, A. Pandikumar, A. Raja, A. Arivarasan, Decoration of CeO<sub>2</sub> nanoparticles on hierarchically porous MnO<sub>2</sub> nanorods and enhancement of supercapacitor performance by redox additive electrolyte, *J. Alloys Compd.* 861 (2021) 158456.
- [25] L. Chen, Q. Wang, X. Wang, Q. Cong, H. Ma, T. Guo, S. Li, W. Li, High-performance CeO<sub>2</sub>/halloysite hierarchical catalysts with promotional redox property and acidity for the selective catalytic reduction of NO with NH<sub>3</sub>, *Chem. Eng. J.* 390 (2020) 124251.
- [26] H. Wang, X. Han, L. Zhang, K. Wang, R. Zhang, X. Wang, S. Song, H. Zhang, Integrating ceria with cobalt sulfide as high-performance electrocatalysts for overall water splitting, *Fundamental Research* 3 (2023) 356–361.
- [27] Q. Dong, B. Wen, X. Zhao, P. Wang, X. Lyu, Electronic structure tailoring of CuCo<sub>2</sub>O<sub>4</sub> for boosting oxygen evolution reaction, *Separ. Purif. Technol.* 353 (2025) 128552.
- [28] A. Popova, E. Sokolova, S. Raicheva, M. Christov, AC and DC study of the temperature effect on mild steel corrosion in acid media in the presence of benzimidazole derivatives, *Corrosion Sci.* 45 (2003) 33–58.
- [29] F.B. Growcock, R.J. Jasinski, Time-resolved impedance spectroscopy of mild steel in concentrated hydrochloric acid, *J. Electrochem. Soc.* 136 (1989) 2310.
- [30] J.R. Macdonald, Impedance spectroscopy, *Ann. Biomed. Eng.* 20 (1992) 289–305.
- [31] D.A. Lopez, S.N. Simison, S. De Sanchez, The influence of steel microstructure on CO<sub>2</sub> corrosion, EIS studies on the inhibition efficiency of benzimidazole, *Electrochim. Acta* 48 (2003) 845–854.
- [32] Z. Stoyanov, B. Grafov, B. Savova-Stoyanova, V. Elkin, *Elektrokhimicheski Impedans*, Nauka, Moscow, 1991.
- [33] M. Salah, S. Azizi, A. Boukhachem, C. Khaldi, M. Amlouk, J. Lamloumi, Effects of lithium doping on: microstructure, morphology, nanomechanical properties and corrosion behaviour of ZnO thin films grown by spray pyrolysis technique, *J. Mater. Sci. Mater. Electron.* 30 (2019) 1767–1785.
- [34] A.K. Ateş, E. Er, H. Çelikkan, N. Erk, Reduced graphene oxide/platinum nanoparticles/naion nanocomposite as a novel 2D electrochemical sensor for voltammetric determination of aliskiren, *New J. Chem.* 41 (2017) 15320–15326.
- [35] Y. Lu, X. Liang, C. Niyungeko, J. Zhou, J. Xu, G. Tian, A review of the identification and detection of heavy metal ions in the environment by voltammetry, *Talanta* 178 (2018) 324–338.
- [36] C.I. Fort, A. Sanou, M. Coulibaly, K.B. Yao, G.L. Turdean, Green modified electrode for sensitive simultaneous heavy metal ions electro detection, *Sensor. Actuator. B Chem.* 418 (2024) 136326.
- [37] T. Yu, S. Li, L. Zhang, F. Li, J. Wang, H. Pan, D. Zhang, In situ growth of ZIF-67-derived nickel-cobalt-manganese hydroxides on 2D V<sub>2</sub>CTx MXene for dual-functional orientation as high-performance asymmetric supercapacitor and electrochemical hydroquinone sensor, *J. Colloid Interface Sci.* 629 (2023) 546–558.
- [38] J. Pan, S. Li, F. Li, W. Zhang, D. Guo, L. Zhang, D. Zhang, H. Pan, Y. Zhang, Y. Ruan, Design and construction of core-shell heterostructure of Ni-V layered double hydroxide composite electrode materials for high-performance hybrid supercapacitor and L-Tryptophan sensor, *J. Alloys Compd.* 890 (2022) 161781.
- [39] W. Alahmad, A. Cetinkaya, S.I. Kaya, P. Varanusupakul, S.A. Ozkan, Electrochemical paper-based analytical devices for environmental analysis: current trends and perspectives, *Trends in Environmental Analytical Chemistry* 40 (2023) e00220.
- [40] I. Azcarate, C. Costentin, C. Methivier, C. Laberty-Robert, A. Grimaud, Electron transfer at the metal oxide/electrolyte interface: a simple methodology for quantitative kinetics evaluation, *J. Phys. Chem. C* 122 (2018) 12761–12770.
- [41] M. Saadaoui, A. Sánchez, P. Díez, N. Raouafi, J.M. Pingarrón, R. Villalonga, Amperometric xanthine biosensors using glassy carbon electrodes modified with electrografted porous silica nanomaterials loaded with xanthine oxidase, *Microchim. Acta* 183 (2016) 2023–2030.
- [42] V. Chandra, K.S. Kim, Highly selective adsorption of Hg<sup>2+</sup> by a polypyrrole-reduced graphene oxide composite, *Chem. Commun.* 47 (2011) 3942–3944.
- [43] U. Andreasson, A. Perret-Liaudet, L.J. van Waalwijk van Doorn, K. Blennow, D. Chiasserini, S. Engelborghs, T. Fladby, S. Genc, N. Kruse, H.B. Kuiperij, L. Kulic, P. Lewczuk, B. Mollenhauer, B. Mroczko, L. Parnetti, E. Vanmechelen, M. Verbeek, B. Winblad, H. Zetterberg, M. Koel-Simmellink, C.E. Teunissen, A practical guide to immunoassay method validation, *Front. Neurol.* 6 (2015) 179.
- [44] S.-S. Li, Q.-Q. Xu, J.-T. Xu, G. Yan, Y.-X. Zhang, S.-W. Li, L.-C. Yin, Engineering Co<sub>2</sub>+ /Co<sup>3+</sup> redox activity of Ni-mediated porous Co<sub>3</sub>O<sub>4</sub> nanosheets for superior Hg(II) electrochemical sensing: insight into the effect of valence change cycle and oxygen vacancy on electroanalysis, *Sensor. Actuator. B Chem.* 354 (2022) 131095.
- [45] X. Zhu, B. Liu, H. Hou, Z. Huang, K.M. Zeinu, L. Huang, X. Yuan, D. Guo, J. Hu, J. Yang, Alkaline intercalation of Ti<sub>3</sub>C<sub>2</sub> MXene for simultaneous electrochemical detection of Cd(II), Pb(II), Cu(II) and Hg(II), *Electrochim. Acta* 248 (2017) 46–57.
- [46] P. Veerakumar, V. Veeramani, S.-M. Chen, R. Madhu, S.-B. Liu, Palladium nanoparticle incorporated porous activated carbon: electrochemical detection of toxic metal ions, *ACS applied materials & interfaces* 8 (2016) 1319–1326.
- [47] W.-Y. Zhou, J.-Y. Liu, J.-Y. Song, J.-J. Li, J.-H. Liu, X.-J. Huang, Surface-electronic-state-modulated, single-crystalline (001) TiO<sub>2</sub> nanosheets for sensitive electrochemical sensing of heavy-metal ions, *Anal. Chem.* 89 (2017) 3386–3394.
- [48] P.-H. Li, Y.-X. Li, S.-H. Chen, S.-S. Li, M. Jiang, Z. Guo, J.-H. Liu, X.-J. Huang, M. Yang, Sensitive and interference-free electrochemical determination of Pb(II) in wastewater using porous Ce-Zr oxide nanospheres, *Sensor. Actuator. B Chem.* 257 (2018) 1009–1020.
- [49] A. Sánchez-Calvo, M.T. Fernández-Abedul, M.C. Blanco-López, A. Costa-García, Paper-based electrochemical transducer modified with nanomaterials for mercury determination in environmental waters, *Sensor. Actuator. B Chem.* 290 (2019) 87–92.
- [50] Y.-F. Sun, J.-J. Li, F. Xie, Y. Wei, M. Yang, Ruthenium-loaded cerium dioxide nanocomposites with rich oxygen vacancies promoted the highly sensitive electrochemical detection of Hg(II), *Sensor. Actuator. B Chem.* 320 (2020) 128355.
- [51] S. Lahrich, B. Maanoun, M.A. El Mhammedi, Electrochemical determination of mercury (II) using NaPb<sub>4-x</sub>Cd<sub>x</sub>(PO<sub>4</sub>)<sub>3</sub> (0 ≤ x ≤ 2) modified graphite electrode: application in fish and seawater samples, *Int. J. Environ. Anal. Chem.* 101 (2021) 140–152.